

Bayesian localization microscopy reveals nanoscale podosome dynamics

Susan Cox^{1,7}, Edward Rosten^{2,3,7}, James Monypenny¹, Tijana Jovanovic-Taliman⁴, Dylan T Burnette⁴, Jennifer Lippincott-Schwartz⁴, Gareth E Jones¹ & Rainer Heintzmann^{1,5,6}

We describe a localization microscopy analysis method that is able to extract results in live cells using standard fluorescent proteins and xenon arc lamp illumination. Our Bayesian analysis of the blinking and bleaching (3B analysis) method models the entire dataset simultaneously as being generated by a number of fluorophores that may or may not be emitting light at any given time. The resulting technique allows many overlapping fluorophores in each frame and unifies the analysis of the localization from blinking and bleaching events. By modeling the entire dataset, we were able to use each reappearance of a fluorophore to improve the localization accuracy. The high performance of this technique allowed us to reveal the nanoscale dynamics of podosome formation and dissociation throughout an entire cell with a resolution of 50 nm on a 4-s timescale.

High-resolution optical microscopy methods have pushed the resolution of a microscope system beyond the Abbe limit by using a nonlinear sample response to illumination light¹. This result is often achieved by switching fluorophores between a dark and a bright state². Stimulated emission depletion (STED) can be used to shrink the effective size of the scanning beam in a confocal system³; saturated structured illumination (SSIM) can extract information hidden in the *moiré* patterns produced when a grating is projected onto the sample⁴; and localization microscopy techniques, such as photoactivatable localization microscopy (PALM)⁵ and stochastic optical reconstruction microscopy (STORM)⁶, build a high-resolution image from the localized positions of many single fluorophores. The application of these techniques to live-cell imaging promises dynamic information on complex protein structures with nanoscale resolution^{7–10}. The ideal microscopy technique would be experimentally simple and fast and would have the property that switching between fluorophore states would not damage the sample. However, several factors still limit the utility of high-resolution microscopy techniques for live-cell imaging applications.

STED requires a specialized microscope and a complex alignment procedure. On live cells, STED has achieved 28 frames per second at 62-nm resolution with low photon numbers over a field of view of

$2.5 \times 1.8 \mu\text{m}$ (ref. 9). As STED is a scanning technique, increasing the field of view decreases the frame rate. SSIM is not limited in this way because it is a wide-field technique; however, SSIM also requires a specialized microscope and can be prone to deconvolution artifacts⁴, and biological high-resolution images obtained using SSIM have not yet been published. Non-saturated structured illumination (SIM) has been carried out at frame rates up to 11 Hz in live cells¹¹ but can provide around 100 nm resolution at most.

Current localization techniques require images in which the fluorescence emission from individual fluorophores does not overlap. This limits the number of fluorophores that can be localized in a given frame and thus the timescale at which useful images of complex structures can be acquired. Achieving the non-overlapping fluorophore emission necessary for conventional localization microscopy analysis requires switching a large fraction of probes into a non-emitting state. This is done either by activating small populations of fluorophores (usually using near-UV light) while imaging with longer wavelengths^{5,6,12} or by keeping a large fraction of the probes in a non-emitting state using relatively high-intensity illumination (kW cm^{-2}) at a single imaging wavelength under suitable chemical conditions^{13,14}. These wavelengths and intensities have been shown to damage live samples¹⁵. Current localization techniques have, however, allowed localization-based imaging of simple structures in live cells at a temporal resolution of 10 s without near-UV activation light⁷ and at a temporal resolution of 0.5 s with near-UV activation light¹⁰.

Another method that uses fluorescence blinking to boost the achievable resolution is called super-resolution optical fluctuation imaging (SOFI) and has been shown to improve images of samples labeled with quantum dots and organic dyes^{16,17}. This method assumes that the blinking of neighboring fluorophores is uncorrelated and uses the temporal correlation between pixels of the image to sharpen the effective point-spread function. Analyzing 1,000-frame datasets of biological samples leads to a 1.4- to 2-fold improvement in resolution¹⁷. There are two other image analysis methods that are able to deal with relatively dense localization data: DAOSTORM¹⁸ and simultaneous multiple emitter fitting¹⁹. These methods can analyze localization

¹Randall Division, King's College London, Guy's Campus, London, UK. ²Department of Engineering, University of Cambridge, Cambridge, UK. ³Computer Vision Consulting Ltd., Lynton House, Woking, Surrey, UK. ⁴National Institutes of Health, Cell Biology and Metabolism Branch, Bethesda, Maryland, USA. ⁵Institute of Physical Chemistry, Friedrich-Schiller University Jena, Jena, Germany. ⁶Institute of Photonic Technology, Jena, Germany. ⁷These authors contributed equally to this work. Correspondence should be addressed to S.C. (susan.cox@kcl.ac.uk).

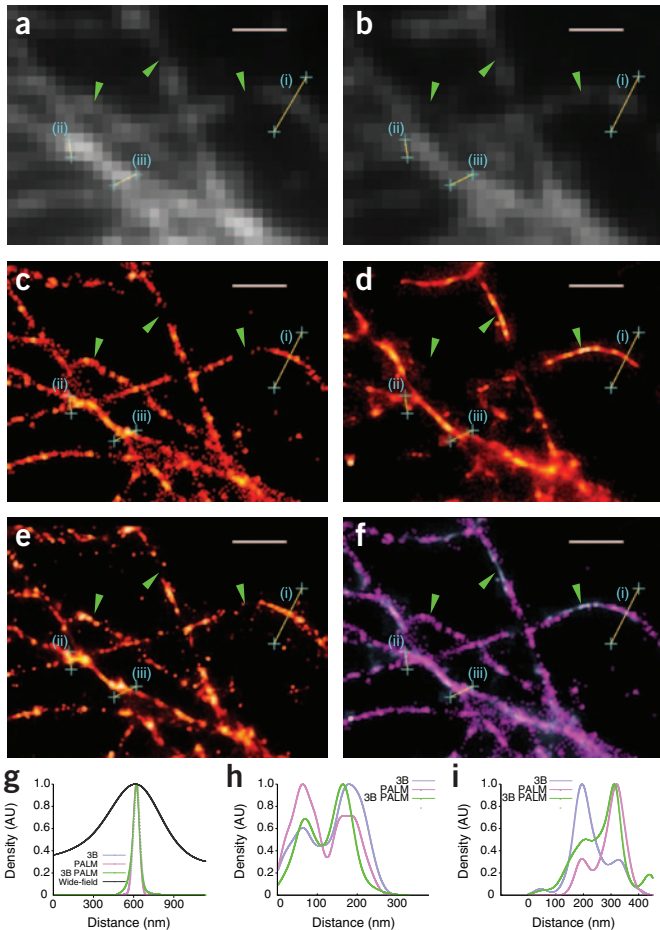


Figure 1 | Correlative measurements using PALM imaging and Bayesian localization imaging on tubulin. **(a,b)** Wide-field images created by averaging all the frames in the PALM image dataset of PA-GFP-tubulin **(a)** and by averaging all of the frames in the Bayesian localization image dataset of mCherry-tubulin **(b)**. **(c,d)** Super-resolution images generated by analyzing the PALM PA-GFP-tubulin dataset from **a** using a standard PALM analysis⁵ **(c)** and by analyzing the mCherry-tubulin dataset from **b** using a 3B analysis **(d)**. **(e)** An image generated from the PALM dataset from **a** using a 3B analysis. **(f)** Overlay of **c** and **d**. Green arrows indicate regions with differences in apparent structure that arise from labeling differences. Linescans corresponding to lines i–iii are shown in **g–i**, respectively, with the 3B analysis data shown in blue, PALM data shown in pink, the 3B analysis PALM data shown in green and the wide-field data shown in black. Scale bars, 1 μm. AU, arbitrary units.

position. This 3B analysis method allowed us to perform localization microscopy with a spatial resolution of 50 nm and a temporal resolution of 4 s on podosomes in living cells expressing a monomeric (m)Cherry fusion of a truncated talin construct. Resolution here is defined as the smallest distance at which two talin strands can be separated, and the localization is defined as the apparent full width at half maximum (FWHM) of a strand of talin. We found that podosomes frequently have a polygonal structure and are highly dynamic over a timescale of tens of seconds.

RESULTS

Standard fluorescent proteins have been shown to blink and bleach in a live-cell environment, even under illumination from standard non-laser light sources. We developed the 3B analysis method to model an entire dataset consisting of a sequence of high-frame-rate images generated from large numbers of fluorescent proteins or other fluorophores undergoing blinking and bleaching processes. We modeled the entire dataset using a factorial hidden Markov model²³. In this Bayesian technique, the state of a system at a certain time point is determined by both a transition matrix and the state of the system at the previous time point. The state of the system is statistically linked to the measured data (the link is not direct, as the measurement process itself is subject to noise). To render the calculation both accurate enough for optimization and algorithmically tractable, we hybridized two hidden Markov model inference methods: the forward algorithm²⁴ and Markov chain Monte Carlo sampling (MCMC) (Online Methods). We calculated many statistical samples of the model parameters, used these samples to generate fluorophore positions and built a probability map of the positions of the fluorophores taken from these samples. Each calculation of a particular set of model parameters used samples of the state taken using MCMC and generated a set of fluorophore positions using a maximum a posteriori (MAP) calculation.

If there were multiple models that fitted the data well, then it was very likely that we had samples of both models. At the end, we marginalized out the fluorophore state to give a distribution of fluorophore positions. Using this method, any ambiguity will cause the final model to be blurred out, making it unlikely that one would report falsely high resolution where there is actually ambiguity (where resolution is defined as the ability to image two fluorophores or line structures as separate). Although there exists only one model that corresponds to the real world, given the data, it is not possible to decide which one this model is, and averaging a multitude of models that are close to being correct seems to be an effective way of representing the underlying structure. A subtle yet key point is that this analysis is integrating over the parameters (both state sequences and

microscopy data that contain some overlapping fluorophores in each image, but they do not use the reappearance of fluorophores to improve localization.

Podosomes are cytoskeletal structures associated with cell adhesion, migration and degradation of the extracellular matrix^{20,21}. They consist of an actin core surrounded by a ring of integrin-associated proteins such as talin and vinculin. This ring was thought to be roughly round, and the podosomes were thought to form and dissociate over a period of about 5–10 min. In wide-field images, the process of formation and dissociation appears as a fading out of the structure²², although we have also seen instances where the podosome appears to slowly unwind.

Here we present a Bayesian localization microscopy method that allows localization data to be extracted from wide-field images of live cells labeled with a standard fluorescent protein. Our method allows the use of data from overlapping fluorophores as well as the use of information from bleaching events, blinking events and changes caused by fluorophores being added or removed in the cell. We carried out high-frame-rate imaging on a standard wide-field microscope with xenon arc lamp illumination. We used a Bayesian technique to model the resulting high-density fluorophore image data as arising from a number of fluorophores, each of which can emit light but which do not necessarily emit light in every frame. By modeling the whole dataset as arising from a number of fluorophores, we were able to use all of the fluorophore reappearances, even those in non-adjacent frames, and thus use all the photons collected from a fluorophore to improve our determination of its

all continuous parameters; see **Supplementary Note**). The output is not a single model; rather, the output is an ensemble of models for different samplings of the state sequences. For each model in the ensemble, the optimized positions of the fluorophores are shown, but these positions are also integrated out when making the determinations of the number of fluorophores in the image. So the outcome of the analysis does not include a specific state sequence; the outcome has integrated over a sampling of different possible state sequences.

Correlative results

To verify that the 3B analysis produces a result that reflects the underlying structure when used on experimental (rather than simulated) data, we performed correlative experiments. We chose to label tubulin because the network of tubulin strands gives rise to strands crossing at many different distances and angles, which allows the resolution to be assessed by determining when the strands can be distinguished. We labeled tubulin with PA-GFP for PALM imaging and with mCherry for Bayesian localization imaging using a 3B analysis (**Fig. 1**). The wide-field images we created by averaging the frames in the two datasets (**Fig. 1a,b**) showed that not all features visible in one dataset are visible in another, as the incorporation efficiencies of mCherry and PA-GFP into the microtubule vary. The incorporation of these proteins into the microtubule was low, so some areas had more mCherry-tubulin and other areas had more PA-GFP-tubulin. Some areas that showed a particularly clear discrepancy between the labeled areas even in the wide-field microscopy images are indicated with green arrows (**Fig. 1a–f**).

Using a 3B analysis, we created a probability map by building up many MAP positions obtained from different samplings of state

sequences (**Fig. 1d**). As a result of the high amount of fluorophore overlap in all the frames, this mCherry data was not analyzable using standard localization microscopy analysis techniques. With the exception of the labeling discrepancies noted above, the 3B analysis results (**Fig. 1d**) were in good agreement with the PALM data (**Fig. 1c**), with features separated by distances as small as 100 nm being visible in both datasets; and when features were present in both datasets, they agreed to a high resolution, as shown in the overlay of the PALM and 3B analysis images (**Fig. 1f**). Additionally, applying the 3B analysis to the PALM dataset yielded a very similar structure as the original PALM analysis (**Fig. 1e**).

Experiments on fixed podosomes

We immunolabeled vinculin in fixed podosome samples with Alexa 488 and mounted the samples in PBS (pH 7.25) with 100 mM 2-mercaptoethanol that we added as a reducing agent to induce blinking¹⁴ (**Supplementary Fig. 1**). We illuminated the sample using a laser at 488 nm with a nominal power of 1 kW cm^{-2} . We collected a series of 300 images, with collection taking a total of 6 s. A video of the raw data is shown as **Supplementary Video 1**. It is notable that there were many overlapping emitting fluorophores in the majority of the frames. This prevented us from using the standard thresholding and fitting-image analysis techniques normally used to reconstruct PALM or STORM images. A typical wide-field image obtained by averaging all 300 images is shown as the background in **Figure 2a**. An example of the MAP positions created from one sampling of the 3B analysis is shown in red in **Figure 2a** (many MAP positions were combined to create the final probability map, shown in **Fig. 2b**).

The apparent thickness of the vinculin strands varied between 6 nm and 60 nm, with the variation probably arising from variation in the number of fluorophore reappearances in different areas, the number of photons detected in one appearance and variations in the distribution of vinculin. The structure of the podosome was geometrical, which is in agreement with recent high-resolution microscopy observations obtained using STED and SIM (at a resolution of approximately 120 nm) (M. Walde, J.M., G.E.J., R.H., S.C., unpublished data). The higher resolution revealed a small structure joining the two podosomes.

We applied the 3B analysis to an entire cell (**Fig. 2c–g**). This application revealed a small number of podosomes with a diameter of less than 300 nm, well below the standard diameter of around 500 nm (**Fig. 2e**), which only appeared as a blob of brightness in the wide-field image. As in SIM and STED studies of podosomes (M. Walde, J.M., G.E.J., R.H., S.C., unpublished data), vinculin strands tended to bind at angles of 120–130° (**Supplementary Fig. 2**).

Experiments on podosomes in living cells

We generated cells from the human acute monocytic leukemia cell line THP1 that stably expressed an mCherry-tagged, truncated talin construct (amino acids 1,974–2,541) using lentiviral gene transduction. The resulting talin mutant comprised the second integrin binding domain of talin and has previously been shown to be an excellent marker of podosome rings in living cells²⁵. We illuminated live samples (maintained at 37 °C) with a mercury arc lamp supplying a nominal power (measured before the objective) of 12 W cm^{-2} to the sample in the wavelength range of 615–687 nm and acquired a series of 5,000 images at 50 frames per second. An example of the data obtained from this experiment is shown as **Supplementary**

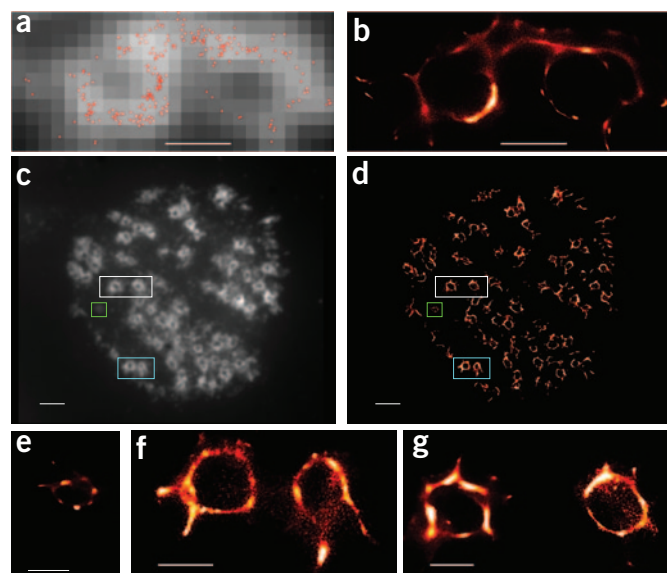


Figure 2 | A 3B analysis of vinculin in fixed cells containing podosomes and labeled with Alexa 488. (a) An example of a maximum likelihood estimate for one set of MCMC samples superimposed on a wide-field image created by averaging all 300 images. (b) A probability map created by combining MAP positions created using different sets of MCMC samples. Scale bars, 500 nm. (c,d) A whole cell showing a wide-field (c) and 3B analysis (d). The green rectangle corresponds to the enlarged image in e, the blue rectangle corresponds to the enlarged image in f, and the white rectangle corresponds to the enlarged image in g. Scale bars, 500 nm (a,b); 2 mm (c,d); and 500 nm (e–g).

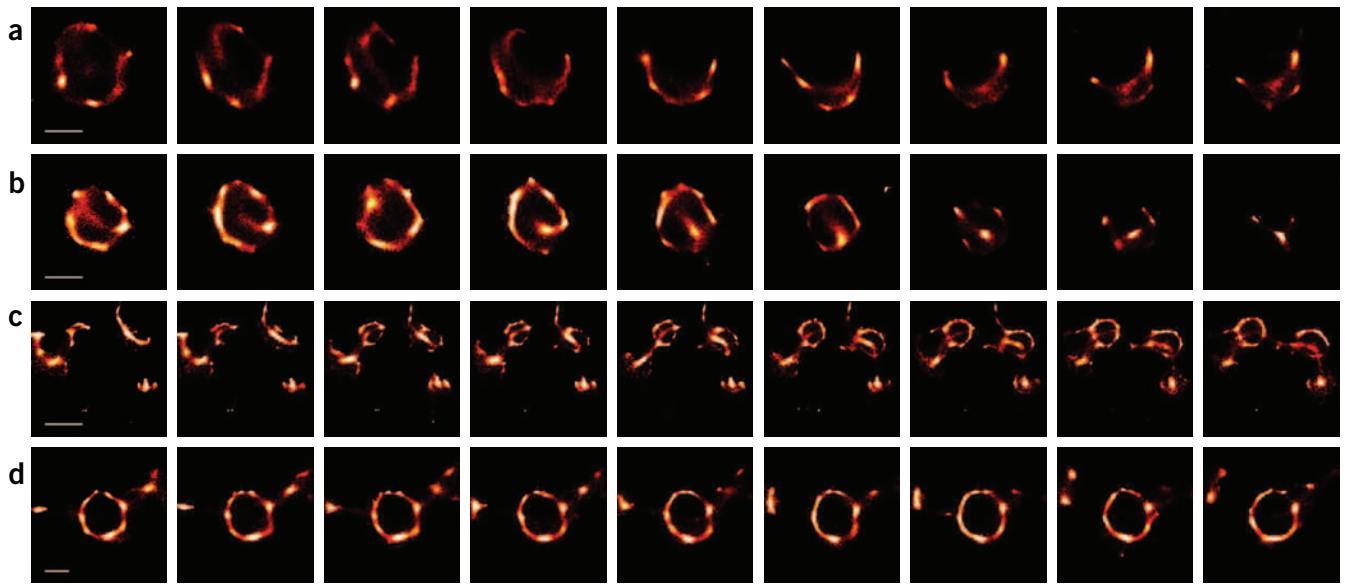


Figure 3 | Podosomes, visualized using an mCherry-tagged truncated talin construct, forming and dissociating in a live cell. **(a,b)** A podosome being dissociated. Scale bars, 400 nm. **(c)** Podosomes being formed. Scale bar, 1 μm . **(d)** A steady-state podosome. Scale bar, 400 nm. Each reconstructed frame used 200 frames (4 s), and frames are spaced 600 frames (12 s) apart. Videos of the podosomes shown in **a–d** are provided as **Supplementary Videos 3–6**, respectively.

Video 2. We applied the 3B analysis to sequences of 200 frames, which corresponds to an acquisition time of 4 s. In **Figure 3**, data are shown for selected time points from the reconstructed image sequence. The complete reconstructed datasets are shown in **Supplementary Videos 3–6**, with the timeshift between video frames being either 50 frames or 0.5 s (though the temporal resolution is still 4 s in these videos).

We determined the localization precision from the FWHM of a linescan that was perpendicular to a talin strand to be as good as 18 nm. We defined the resolution as the distance at which two talin strands could be visually separated, as measured by a linescan. We determined the resolution here to be 50 nm (**Supplementary Fig. 3**).

Movement of the fluorophores will cause an analysis to produce an image that is smeared in the direction of the movement. This effect limits the resolution that is achievable if structures are moving

by distances larger than the resolution of the system on time-scales smaller than the acquisition time for a single reconstructed high-resolution image. We chose podosomes as a suitable test system for our imaging analyses, as they form and dissociate over a period of several minutes, and most podosomes do not appear to move around the cell during this time (if podosome movement is observed, it is generally restricted to a few hundred nm).

We observed podosomes undergoing assembly and two different modes of breakdown. In the first mode of podosome breakdown, the podosome shows a small break, and then one end of the break gradually retracts, producing an ‘unwinding’ effect (**Fig. 3a**). This retraction seems to be associated with the formation of small (250 nm in diameter) struts in the region of the cell where the podosome is being dissociated. In the second mode of podosome dissociation, struts (approximately 450 nm in length) repeatedly form

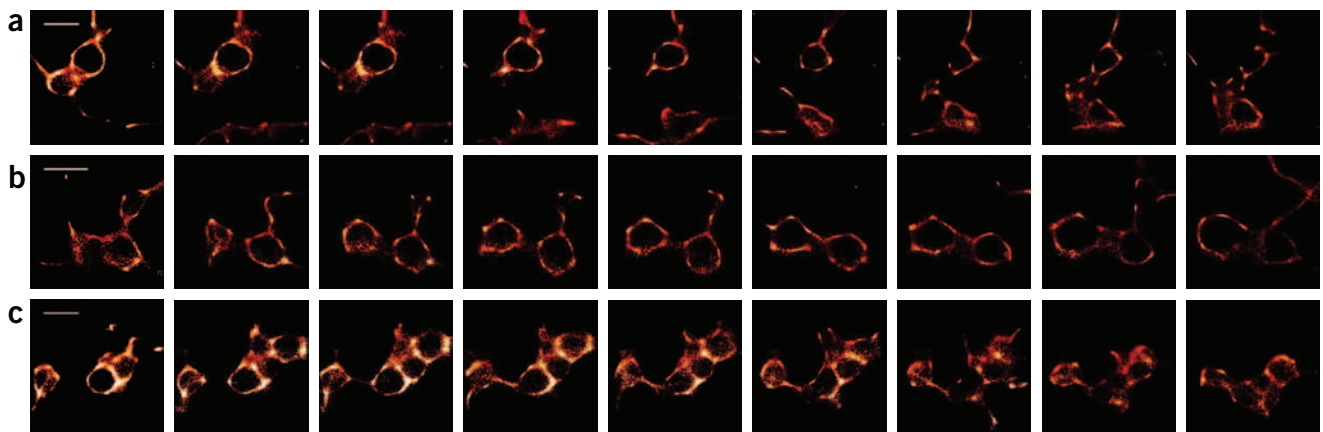


Figure 4 | Dissociation and formation of groups of podosomes in a motile cell. **(a,b)** Dissociation and formation of linked podosomes. **(c)** Separated podosomes joining together. Each reconstructed frame used 200 frames (4 s), and frames are spaced 1,000 frames (20 s) apart. A video containing the podosomes shown in **a–c** as well as the rest of the cell is provided as **Supplementary Video 7**. Scale bars, 800 nm.

across the podosome, drawing the talin in to a central point until it has been removed (Fig. 3b). We also observed podosome formation in which the strut seemed to have a crucial function, with the podosome nucleating from a strut and then expanding on either side of it (Fig. 3c). Once the podosome had formed and the strut had served its purpose, it appeared to be broken down. Some podosomes showed no apparent changes in the wide-field image and were relatively stable at the nanoscale (Fig. 3d).

We also observed more complex structures composed of a number of joined podosomes and struts. Imaging of a motile cell revealed highly dynamic behavior of these complex structures, with podosome structures changing on a timescale of tens of seconds. Figure 4 depicts one example of such behavior, where two groups of podosomes become joined after each group extends a strut. Where the two struts join, a miniature podosome-like structure forms, and the two groups of podosomes are pulled closer together. We saw similar behavior across the whole cell (Supplementary Video 7).

To determine whether the truncated talin construct that we used for our live-cell imaging experiments is representative of the structure of the podosome protein ring, we performed two-color measurements in fixed cells. We fixed cells expressing the mCherry-tagged truncated talin construct, and we immunolabeled vinculin with Alexa 488-tagged secondary antibody. We used the same embedding conditions that we used for the other fixed-cell experiments. The truncated talin construct and the vinculin had similar distributions (Fig. 5). The vinculin image was localized slightly more to the periphery of the ring, and the talin was more localized to the center, whereas the short strands at the edge of the ring were more visible in the vinculin. This hints that the localization of different proteins in the ring are subtly different and shows that the 3B analysis method can be used to build a map of the spatial organization of different podosome components.

Simulations

To further validate the Bayesian localization imaging results from our 3B analysis method, we analyzed simulated datasets. Bayesian fitting methods use wide priors over a large number of parameters to fit real-world data, which tend to have narrow, unknown distributions over these parameters. Simulations created using the fitting distributions may not provide good results, so we created simulated datasets by using blinking sequences and fluorophore positions from the PALM correlative data. We created each simulated frame using the fluorophore positions from 16 PALM frames (Fig. 6). The average separation of two nearest-

Figure 6 | Simulations showing the performance of the 3B analysis method. (a–d) Ground truth simulated image data (a,b) and 3B analysis reconstructions (c,d). (e–h) For the simulations, the simulated wide-field image created by averaging all frames (e,f) and a typical frame (g,h) are shown. Images in a and c correspond to the boxed regions in e and g, respectively. (i,j) Linescans of the simulations and 3B analysis reconstructions show the 3B analysis method achieving good reproduction of the structure and a resolution of 50 nm. Scale bars, 50 nm (a,c); otherwise, 200 nm.

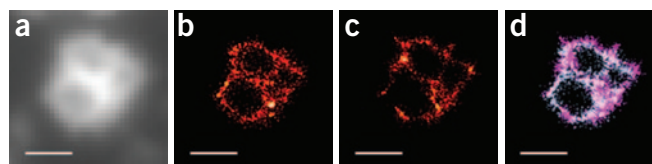


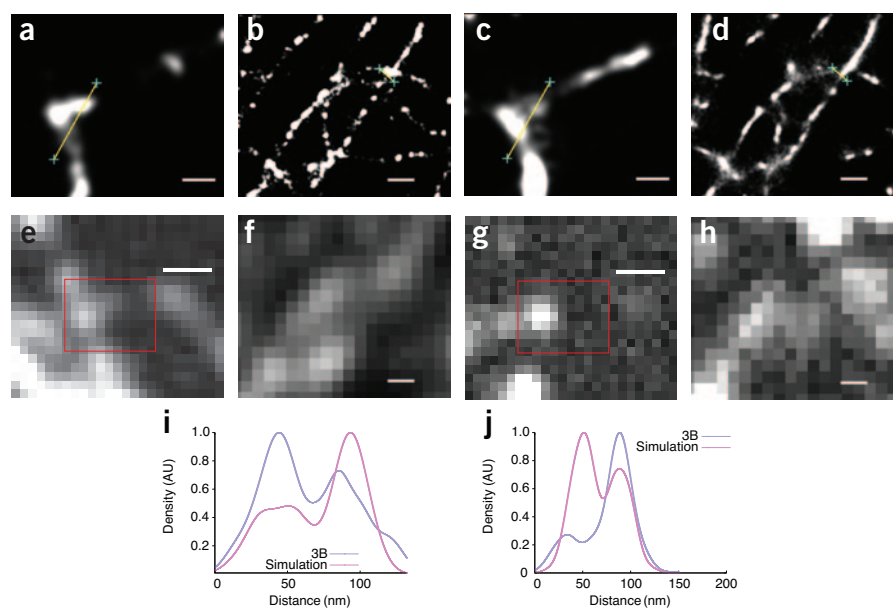
Figure 5 | A 3B analysis of fixed-cell data to determine the colocalization of vinculin and the truncated talin construct in podosomes. (a) Wide-field image of vinculin labeled with Alexa 488. (b,c) The individual 3B analysis images shown in glowscale for talin (b) and vinculin (c). (d) Superposition of images from the 3B analysis showing the truncated talin construct (in cyan) and vinculin 3B data (in magenta). Scale bars, 1 μ m.

neighbor fluorophores was 112 nm, which is considerably smaller than the point spread function FWHM (270 nm), leading to a large amount of fluorophore overlap in simulated the frames (Fig. 6g,h).

The simulations showed that the 3B analysis method achieves 50-nm resolution at an intersection of two strands (Figs. 6i,j). This method produced the correct structure but did not pick up every fluorophore. We observed artificial thinning and thickening of the structures in different areas, but the magnitude of all of these effects was less than 20 nm. In all instances, the intensity between close spots was somewhat enhanced, making the spots appear more 'connected' than they were in the PALM data. This enhanced intensity suppressed the resolution along a line of fluorophores compared to the resolution perpendicular to a line of fluorophores. We quantified the resolution perpendicular to lines of fluorophores in all our experiments.

DISCUSSION

The 3B analysis method removes a number of barriers to getting the good localization information that can be obtained using other approaches. The experiments for 3B analysis are easy to implement: live cell experiments use fluorescent proteins, a wide-field microscope and arc lamp illumination, which are all standard in most cell biology labs. With this equipment, it is possible to achieve a 50-nm resolution with data from only a few seconds of acquisition, and it is possible to image for extended time periods. The software that we used to perform the analysis here is provided in the Supplementary



Software; updated versions of the software can be obtained from <http://3bmicroscopy.com>.

The computational effort of our method is linear with respect to the number of fluorophores multiplied by the number of pixels. For a cell such as that shown in **Figure 2**, we modeled the data as arising from 10,000 fluorophores, and we used 200 sets of MCMC samples to build the probability map.

To analyze a region of around $1.5 \times 1.5 \mu\text{m}$ in size, processing on a single core i7 (3.33 GHz) for 6 h is required. Larger areas can be analyzed, but the time required for these analyses scales with the area of the region. To analyze large areas, the analysis is broken down into a number of small areas. To analyze large images or video data, a cluster computer is required.

Our method has a natural mechanism for trading off temporal and spatial resolution: analyzing more frames simultaneously raises the spatial resolution but lowers the temporal resolution. Comparing our method to SOFI, both methods can deal with images that have overlapping fluorophores, but SOFI requires more data and delivers a more limited resolution improvement than the 3B analysis. In the 3B analysis, it is possible to artificially sharpen structures by including models with fewer fluorophores than the data, but in simulations, we found these effects to be considerably below the resolution limit.

Rather than revealing an improved resolution picture of an apparently smooth process in podosomes, achieving high resolution revealed an entirely new level of complexity. Podosomes were previously thought to smoothly form and dissociate over a period of several minutes²². However, our results indicate that podosomes are highly dynamic structures. It appears that smaller ring-type structures down to 230 nm play a crucial part in podosome dynamics. Rather than strands simply being parts of partially grown podosomes, our results indicate that these structures may have a role in seeding new areas of podosomes. In another form, as struts spanning across a podosome, they appear to be associated with podosome formation and dissociation.

Our use of standard fluorescent proteins opens the techniques of high spatial and temporal resolution microscopy to a whole new range of samples. Many of these samples, like podosomes, may be complex all the way down to the nanoscale.

METHODS

Methods and any associated references are available in the online version of the paper at <http://www.nature.com/naturemethods/>.

Note: Supplementary information is available on the Nature Methods website.

ACKNOWLEDGMENTS

We acknowledge helpful discussions with A. Fraser, F. Viola, P. Fox-Roberts, O. Mandula and J. Sleep. We thank M. Kielhorn for assistance in aligning the optical system and K. Gloer for critical reading of the manuscript. We thank M. Parsons (King's College London) for providing the template plasmid. We acknowledge support from the EU Seventh Framework Programme (FP7 Project GA 215597 (S.C. and R.H.), EU FP7 Project ITN 237946 T3Net (G.E.J.)), the Wellcome Trust (S.C., J.M. and G.E.J.), the Medical Research Council (UK) (G.E.J.) and the Royal Society (S.C.).

AUTHOR CONTRIBUTIONS

S.C., J.M., T.J.-T., D.T.B., J.L.-S., G.E.J. and R.H. conceived of and designed the experiments. S.C. and E.R. conceived of and designed the analysis. J.M. prepared the podosome samples, and T.J.-T. and D.T.B. prepared the samples for correlative measurements. S.C. and J.M. performed live-cell experiments, S.C. carried out

fixed-cell experiments on podosomes, and T.J.-T. and D.T.B. carried out the correlative measurements. E.R. and S.C. carried out the data analysis and wrote the manuscript, and all authors revised the manuscript.

COMPETING FINANCIAL INTERESTS

The authors declare no competing financial interests.

Published online at <http://www.nature.com/naturemethods/>.

Reprints and permissions information is available online at <http://www.nature.com/reprints/index.html>.

- Heintzmann, R. & Ficz, G. Breaking the resolution limit in light microscopy. *Methods Cell Biol.* **81**, 561–580 (2007).
- Hell, S.W. Microscopy and its focal switch. *Nat. Methods* **6**, 24–32 (2009).
- Klar, T.A., Jakobs, S., Dyba, M., Egner, A. & Hell, S.W. Fluorescence microscopy with diffraction resolution barrier broken by stimulated emission. *Proc. Natl. Acad. Sci. USA* **97**, 8206–8210 (2000).
- Heintzmann, R., Jovin, T.M. & Cremer, C. Saturated patterned excitation microscopy—a concept for optical resolution improvement. *J. Opt. Soc. Am. A* **19**, 1599–1609 (2002).
- Betzig, E. *et al.* Imaging intracellular fluorescent proteins at nanometer resolution. *Science* **313**, 1642–1645 (2006).
- Rust, M.J., Bates, M. & Zhuang, X. Sub-diffraction-limit imaging by stochastic optical reconstruction microscopy (STORM). *Nat. Methods* **3**, 793–796 (2006).
- Wombacher, R. *et al.* Live-cell super-resolution imaging with trimethoprim conjugates. *Nat. Methods* **7**, 717–719 (2010).
- Shroff, H., Galbraith, C.G., Galbraith, J.A. & Betzig, E. Live-cell photoactivated localization microscopy of nanoscale adhesion dynamics. *Nat. Methods* **5**, 417–423 (2008).
- Westphal, V. *et al.* Video-rate far-field optical nanoscopy dissects synaptic vesicle movement. *Science* **320**, 246–249 (2008).
- Jones, S.A., Shim, S.-H., He, J. & Zhuang, X. Fast, three-dimensional super-resolution imaging of live cells. *Nat. Methods* **8**, 499–505 (2011).
- Kner, P., Chhun, B.B., Griffis, E.R., Winoto, L. & Gustafsson, M.G.L. Super-resolution video microscopy of live cells by structured illumination. *Nat. Methods* **6**, 339–342 (2009).
- Heilemann, M., Dedecker, P., Hofkens, J. & Sauer, M. Photoswitches: key molecules for subdiffraction-resolution fluorescence imaging and molecular quantification. *Laser Photonics Rev.* **3**, 180–202 (2009).
- Zhuang, X. Nano-imaging with STORM. *Nat. Photonics* **3**, 365–367 (2009).
- Heilemann, M., van de Linde, S., Mukherjee, A. & Sauer, M. Super-resolution imaging with small organic fluorophores. *Angew. Chem. Int. Ed.* **48**, 6903–6908 (2009).
- Lippincott-Schwartz, J. & Manley, S. Putting super-resolution fluorescence microscopy to work. *Nat. Methods* **6**, 21–23 (2009).
- Dertinger, T., Colyera, R., Iyera, G., Weissa, S. & Enderleind, J. Fast, background-free, 3D super-resolution optical fluctuation imaging (SOFI). *Proc. Natl. Acad. Sci. USA* **106**, 22287–22292 (2009).
- Dertinger, T., Heilemann, M., Vogel, R., Sauer, M. & Weiss, S. Superresolution optical fluctuation imaging with organic dyes. *Angew. Chem.* **122**, 9631–9633 (2010).
- Holden, S., Uphoff, S. & Kapanidis, A. DaoSTORM: an algorithm for high-density super-resolution microscopy. *Nat. Methods* **8**, 279–280 (2011).
- Huang, F., Schwartz, S.L., Byars, J.M. & Lidke, K.A. Simultaneous multiple-emitter fitting for single molecule super-resolution imaging. *Biomedical Optics Express* **2**, 1377–1393 (2011).
- Linder, S. & Aepfelbacher, M. Podosomes: adhesion hot-spots of invasive cells. *Trends Cell Biol.* **13**, 376–385 (2003).
- Linder, S. & Kopp, P. Podosomes at a glance. *J. Cell Sci.* **118**, 2079–2082 (2005).
- Monyppenny, J. *et al.* Role of WASP in cell polarity and podosome dynamics of myeloid cells. *Eur. J. Cell Biol.* **90**, 198–204 (2011).
- Ghahramani, Z. & Jordan, M.I. Factorial hidden Markov models. *Mach. Learn.* **29**, 245–273 (1997).
- Rabiner, L.R. A tutorial on hidden Markov models and selected applications in speech recognition. *Proc. IEEE* **77**, 257–286 (1989).
- Wiesner, C., Faix, J., Himmel, M., Bentzien, F. & Linder, S. KIF5B and KIF3A/KIF3B kinesins drive MT1-MMP surface exposure, CD44 shedding, and extracellular matrix degradation in primary macrophages. *Blood* **116**, 1559–1569 (2010).

ONLINE METHODS

Sample preparation for correlative measurements. B16-F1 cells were seeded on coverslips coated with $25 \mu\text{g ml}^{-1}$ laminin as previously described²⁶. Cells were then co-transfected with PA-GFP-tubulin and mCherry-tubulin with FuGENE 6 (Roche) following the manufacturer's recommendations. Cells were fixed with 4% paraformaldehyde, 0.2% glutaraldehyde (Electron Microscopy Sciences) in PBS (pH 7.4) for 35 min at room temperature (18–25 °C). Streaming time-lapse images were acquired with an Olympus IX71 total internal reflection fluorescence microscope using a 60 \times , 1.45-numerical-aperture (NA) objective (Olympus), and fluorescence emission was detected with an electron-multiplying charge-coupled device (EM-CCD) camera (Andor Technology, DV887ECS-BV). PA-GFP constructs were imaged with 100 ms integration times (488-nm laser power was 400–800 μW going into the microscope). mCherry constructs were imaged with 50-ms integration times (561 nm laser power was 1 mW going into the microscope). PALM datasets comprised 5,000 frames, 3B datasets comprised 1,000 frames, and both datasets were corrected for drift. For the PALM data, single molecules were fitted with theoretical Gaussians, and PALM images were reconstructed as previously described⁵.

Sample preparation for podosome observations. The THP1 cell line, which can be stimulated to differentiate into macrophages, was used to observe podosomes. Podosome formation was induced in these cells by seeding them on fibronectin-coated cover glasses in the presence of the cytokine TGF- β 1 (1 ng ml⁻¹). Vinculin staining was conducted using VN-1 vinculin mouse monoclonal antibody (Sigma) conjugated to Alexa 488 mouse secondary antibody. Coverslips were mounted in PBS (pH 7.4) containing 100 mM 2-mercaptoethanol to induce blinking at a suitable rate¹⁴.

Lentiviral-mediated gene transduction of THP1 cells. PCR was used to amplify cDNA encoding residues 1,975–2,541 of human talin from a template plasmid. The resulting sequence was cloned using the Zero Blunt vector (Invitrogen) into the multiple cloning site of the pLNT/Sffv-mCherry-MCS vector generating the mCherry-talin (1,975–2,541) lentiviral expression construct. VSV-G pseudotyped lentivirus encoding mCherry-talin (1,975–2,541) was packaged in 293T cells by transient transfection of the cells with the p Δ 8.91 and pMD.G accessory plasmids along with the pLNT/Sffv transfer vector encoding the talin construct. Supernatants containing lentivirus were harvested 48 h after transfection, filtered through a 0.45- μm -pore-size filter and stored at -80 °C. THP1 cells were transduced with lentivirus by incubation with lentiviral supernatants for 24 h, then washed using sequential centrifugation and resuspension steps and left for an additional 3 d to express the fusion protein. Twenty-four hours before the live-cell imaging experiments, THP1 cells were seeded at a density of 2.5×10^6 cells per ml on fibronectin-coated ($10 \mu\text{g ml}^{-1}$) glass coverslips in the presence of 1 ng ml⁻¹ TGF- β to induce cell attachment and podosome formation. For all imaging experiments, coverslips with adherent cells were mounted onto purpose-built glass viewing chambers. For the two-color experiments, cells containing the truncated mCherry-talin construct were fixed and stained as described previously.

Microscopy for the podosome experiments. For the fixed-cell experiments, a wide-field Zeiss Axiovert 200M microscope was used with an oil immersion objective (63 \times , NA 1.4; Zeiss) and a

2.5 \times Optovar. Illumination was provided by an argon ion laser (Innova 90 coherent) emitting at 488 nm. Images were recorded using a Cascade II EM-CCD camera (Photometrics) with square pixels and a pixel pitch of 16 μm (each recorded pixel corresponds to 102 nm in real space). The frame rate varied between 50 and 60 frames per second.

For the live-cell experiments, a wide-field Olympus IX81 was used with an oil immersion objective (100 \times , NA 1.4; Olympus). Illumination was provided by a Sutter Lambda LS xenon arc lamp coupled with a liquid light guide, with a Comar GFP-RFP filter set (for RFP, excitation was at 537.5–592.5 nm, emission was at 615–687 nm and dichroic was at 590–700 nm). Images were recorded using a Cascade II EM-CCD camera (with the same properties as the camera described above). For **Figure 3**, no post magnification was used, meaning each recorded pixel corresponded to 160 nm in real space. For **Figure 4**, a 1.6 \times post magnification was used, meaning that each recorded pixel corresponded to 100 nm on the sample. The drift in these experiments was assessed by monitoring the drift of the bead samples over time. The beads were imaged using the same frame rate and for the same amount of time as in the live-cell experiment. The drift was found to be within the localization error, with the mean of the localization position varying by up to 10 nm over 5,000 images (acquired over 98 s). We therefore ignored drift effects in our analysis, as the expected drift over the 200 images that we used to reconstruct an image was expected to be 0.4 nm.

Simulations. Simulations were created using fluorophore positions from 4,800 out of the 5,000 PALM frames, with each simulated frame created from 16 PALM frames, resulting in 300 simulated frames. The simulated frames were created from two groups of PALM frames such that simulated frame 0 consisted of PALM frames 0–7 and 2,400–2,407, simulated frame 1 consisted of PALM frames 8–15 and 2,408–2,415 and so on. This method prevented later frames from becoming unrealistically sparse. The FWHM of the simulated point spread function was set to 1.56 pixels, which corresponds to a FWHM of 270 nm at 86 nm per pixel (this halved the number of nm per pixel compared to the original PALM dataset, but because the positions of the fluorophores were set relative to pixels, it also decreased the distance between fluorophores by a factor of 2). This created datasets with overlapping fluorophores. Simulated images were created using Gaussian-shaped spots of average brightness 1,200 photons on a background of average brightness 600 photons with Poisson noise. The photon counts and, therefore, the signal-to-noise ratio was set using photon counts from the background and isolated fluorophores in the fixed-cell dataset.

Analysis. The image series was modeled using a factorial hidden Markov model²³ as arising from a number of fluorophores. Each fluorophore was modeled using a Markov model that had three possible states: emitting (light), non-emitting and bleached. The fluorophore can transfer between the emitting and non-emitting states and can also transfer from the non-emitting to the bleached state. Once in the bleached state, the fluorophore cannot leave it. The state transition diagram for fluorophores is shown in **Supplementary Figure 4**. From our estimates of the lifetimes and transition probabilities associated with the energy levels^{14,27} and the frame time of around 0.02 s, we calculated estimates for all the model probabilities in a given frame. We obtained values of $P_1 = 0.16$, $P_2 = 0.84$, $P_3 = P_4 = 0.495$ and $P_5 = 0.01$ (see **Supplementary Fig. 4** and **Supplementary Note**

for definitions and discussion of these probabilities). To calculate these values, the typical values of the lifetimes and various transition probabilities were taken. The on-state lifetime was taken to be 10^{-7} s, and a fluorophore was taken to be 10^5 times more likely to remain in the on state than to transition to the off state. The frame rate of the camera was taken to be between 50 and 60 Hz (each frame takes 18 ms). So each frame is 18,000 on-state lifetimes, in each of which the fluorophore had a probability of 0.99999 of returning to the on state. The values of P_3 and P_4 were taken with a variety of typical off-state lifetimes (10^{-3} – 10^{-2} s) assuming a monoexponential decay. This led to values of P_4 between 0.1 and 0.8. The value of 0.495 was chosen as being reasonably central to this spread, given the large uncertainties in the input values.

The same state transition probabilities were used for fitting both fixed-cell and live-cell datasets, as only a broadly correct prior is needed for this type of modeling. The structure observed in the reconstructed image did not vary to an extent that it altered the observed structure if the state transition probabilities were varied within physically realistic values. We assume that neighboring fluorophore states are statistically completely independent. Our results are only weakly dependent on the priors. Without blinking or bleaching, this method would have the same limits as deconvolution. To enhance the blinking, a switching probe with better dynamics could be used.

We calculated the relative probability that a fluorophore was present compared to the null hypothesis that the data arose from noise. The model evidence for each hypothesis can be calculated by integrating out over state sequences (the blinking and bleaching state in each frame) using the forward algorithm²⁴ and by integrating out over continuous variables using Laplace's approximation²⁸. However, the forward algorithm calculation is exponential in the number of fluorophores. An alternative approach is to take a statistical sample of state sequences, but this method does not provide sufficiently accurate results. We therefore used a hybrid of the forward algorithm and a state-sampling technique. A detailed description of the algorithm is given in the **Supplementary Note**.

The algorithm is then run on user-selected areas. The user must specify the pixel size (which is used to calculate the predicted point spread function size) and the starting number of fluorophores in the area. The final result of the algorithm is a density map of the positions of fluorophores yielded. Further details on the parameters and reconstruction algorithm are given in the **Supplementary Note**.

26. Burnette, D.T. *et al.* A role for actin arcs in the leading-edge advance of migrating cells. *Nat. Cell Biol.* **13**, 371–382 (2011).
27. Xie, X.S. Optical studies of single molecules at room temperature. *Annu. Rev. Phys. Chem.* **49**, 441–480 (1998).
28. MacKay, D.J.C. *Information Theory, Inference, and Learning Algorithms* (Cambridge Univ. Press, 2003).